# Molecular Insights into the Surface Morphology, Layering Structure, and Aggregation Kinetics of Surfactant-Stabilized Graphene Dispersions

Shangchao Lin,[†,‡,§] Chih-Jen Shih,[†,§] Michael S. Strano,[†] and Daniel Blankschtein[*,†]

[†]Departments of Chemical and [‡]Mechanical Engineering, Massachusetts Institute of Technology, Cambridge, Massachusetts 02139, United States

S *Supporting Information*

ABSTRACT: The production of graphene with open band gaps for the manufacturing of graphene-based electronic and optical devices requires synthesis methods to either control the number of layers to enrich AB-stacked bilayer or trilayer graphene or control the extent of functionalization of monolayer graphene. Solution-phase dispersion of graphene is promising for both methods to create printable electronics and nanocomposites. However, both methods face common challenges, including controlling the surface morphology, reducing the turbostratic layering, and enhancing the dispersion stability. To address these challenges at the molecular level, we successfully combined molecular simulations, theoretical modeling, and experimental measurements. First, we probed the surface structure and electrostatic potential of monolayer graphene dispersed in a sodium cholate (SC) surfactant aqueous solution, which exhibits 2D sheets partially covered with a monolayer of negatively charged cholate ions. Similar to the case of carbon nanotube functionalization, one may regulate the binding affinity of charged reactants for graphene functionalization by manipulating the surface morphology. Subsequently, we quantified the interactions between two graphene—surfactant assemblies by calculating the potential of mean force (PMF) between two surfactant-covered graphene sheets, which confirmed the existence of a metastable bilayer graphene structure due to the steric hindrance of the confined surfactant molecules. The traditional Derjaguin—Landau—Verwey—Overbeek (DLVO) theory was found to be adequate to explain the long-range electrostatic repulsions between the ionic surfactant-covered graphene sheets but was unable to account for the dominant, short-range steric hindrance imparted by the confined surfactant molecules. Interestingly, one faces a dilemma when using surfactants to disperse and stabilize graphene in aqueous solution: on the one hand, surfactants can stabilize graphene aqueous dispersions, but on the other hand, they prevent the formation of new AB-stacked bilayer and trilayer graphene resulting from the reaggregation process. Finally, the lifetime and time-dependent distribution of various graphene layer types were predicted using a kinetic model of colloid aggregation, and each graphene layer type was further decomposed into subtypes, including the AB-stacked species and various turbostratic species. The kinetic model of colloid aggregation developed here can serve as a useful tool to evaluate the quality of graphene dispersions for subsequent substrate-transferring or functionalization processes.
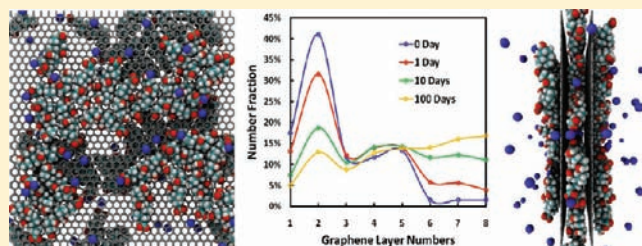
1. INTRODUCTION

Graphene, a two-dimensional, one-atom-thick hexagonal lattice of carbon atoms,[1] has generated considerable attention as a result of its outstanding electronic, mechanical, optical, thermal, and chemical properties.[2] While the earliest graphene samples were produced using micromechanical cleavage from highly ordered pyrolytic graphite (HOPG),[1,3] significant effort has been devoted in recent years to develop larger-scale methods to produce graphene. Such methods involve two main approaches: direct chemical growth of graphene on substrates (e.g., chemical vapor deposition, CVD)[4,5] and direct exfoliation of graphene from naturally occurring graphite flakes in various solvents.[6,7] The latter, solution-phase method offers several significant advantages since it: (i) utilizes inexpensive and readily available graphite flakes, (ii) does not require transferring the graphene from the growth substrate, (iii) employs existing technologies (e.g., sonication and centrifugation) for scaled-up large volume processing, and (iv) allows solution-phase chemical functionalization of graphene.[6]

Among various available solvents, the use of water avoids the toxic polar organic solvents (e.g., NMP[8] and DMF[9]) and allows the use of graphene for biological applications, including molecular sensors and transistors.[10−12] Due to the hydrophobic nature of pristine graphene, the use of surfactants is essential to assist in the dispersion of graphene in an aqueous phase. It was recently demonstrated that graphite flakes (from inexpensive graphite powder) can be exfoliated and dispersed into pristine, unfunctionalized graphene sheets in aqueous media using the conventional linear ionic surfactant sodium dodecylbenzene sulfonate

ACS Publications   © 2011 American Chemical Society

12810   dx.doi.org/10.1021/ja2048013 | *J. Am. Chem. Soc.* 2011, 133, 12810–12823

(SDBS), with the aid of bath sonication and centrifugation.[13] The electrostatic repulsions between the SDBS-covered graphene sheets were quantified experimentally by measuring the zeta potential of the graphene—SDBS assemblies using electrophoresis.[13] Very recently, the bile salt surfactant, sodium cholate (SC), has also been utilized to disperse graphene in aqueous solution at high concentrations.[14] Moreover, Green et al. utilized horn ultrasonication and density gradient ultracentrifugation (DGU) to isolate SC-stabilized graphene with controlled thickness.[15] However, the graphene dispersions reported in ref 15 were found to be turbostratic (non-AB stacked) after DGU, as quantified using Raman spectroscopy.

It is well-known that solution-phase graphene dispersions are polydisperse with various layer numbers and interlayer registrations (layering structure), where these characteristics determine the electronic and optical properties.[16] For multilayer graphene, the Bernal AB-stacking found in natural graphite is the most energetically favorable structure. More importantly, AB-stacked multilayer, most notably, bilayer and trilayer, graphene has properties that are distinct from those of monolayer graphene (which is a semimetal with zero band gap). This is because bilayer and trilayer graphene exhibit tunable band gaps in response to applied gate bias or external electric fields,[17,18] thus imparting great flexibility in the design and optimization of electronic and optical devices. However, the solution-phase exfoliated bilayer and trilayer graphene sheets after DGU exhibit primarily a turbostratic, non-AB-stacking structure, as quantified using Raman spectroscopy.[15] This is similar to what is observed in CVD—graphene samples and those grown on SiC[19] and suggests disordering of the graphene sheets due to the weak interlayer coupling. As a result, most of the multilayer graphenes, except for those produced using micromechanical cleavage, are turbostratic, where slight deviations from the AB-stacking destroy the unique electronic structures of bilayer and trilayer graphene and renders them electronically similar to monolayer graphene.[20] For example, theoretical analysis has predicted that an external electric field, applied normal to the turbostratic bilayer graphene, cannot open an electronic band gap.[21] Therefore, understanding the formation of the turbostratic layering structure of multilayer graphene is very important to improve the solution-phase exfoliation process. If layering can be controlled during exfoliation, this would provide a viable route for the mass production of AB-stacked multilayer graphene on arbitrary substrates for electronic devices. When combined with the well-developed intercalation chemistry of graphite,[22] it becomes possible to obtain graphene dispersions with layering control. Graphene sheets from covalent graphite intercalation compounds (GICs),[23−25] ionic GIC,[26−28] and expanded graphite (EG)[29] have been reported. Very recently, our group successfully utilized Stage-2 and Stage-3 ionic GICs to produce AB-stacked bilayer- and trilayer-enriched graphene dispersions with the aid of slow homogenization and mild centrifugation, respectively.[30]

Another notable approach to modify the electronic properties (e.g., opening band gaps) of graphene is to covalently functionalize the surface of graphene with special reactants.[31,32] The source for functionalization can be either from defect-free graphene from micromechanical exfoliation,[1,3] CVD growth,[4,5] and solution exfoliation,[13,15] or from reduced graphene oxides (GOs) which are produced from graphite oxidation and have many defects (also referred to as chemically converted graphene, CCG).[32] The extent of reaction of graphene with the reactants, most notably, diazonium salts, is largely controlled by the

amounts of available reaction sites on the graphene surface,[31] similar to the functionalization of single-walled carbon nanotubes (SWNTs).[33] Since most of the reactions take place in aqueous media, anionic surfactants are usually added to either disperse graphene before functionalization[32] or accelerate the reaction process by concentrating the diazonium cations near the graphene surface.[31] According to the two-step reaction mechanism proposed by Usrey et al.,[34] the only selective step in the functionalization process of SWNTs is not the actual reaction, but the adsorption of reactants to the available binding sites on the surfactant-covered SWNT surface. If we draw analogies between SWNT and graphene, then the available reaction sites should be determined by the surfactant surface coverage. In addition, the adsorption of the diazonium cations onto the ionic surfactant-covered graphene surface should also be greatly affected by the sign of the charge of the surfactant molecules due to electrostatic interactions.

In spite of the extensive experimental reports on solution-phase graphene production and functionalization, to date, a molecular understanding of the surface morphology of monolayer and multilayer graphene—surfactant assemblies has not been developed. In addition, the origin of the turbostratic multilayer graphene structure following the DGU process in the work by Green et al. has not been elucidated.[15] Furthermore, the mechanism underlying the dispersion stability and aggregation kinetics of surfactant-stabilized graphene, produced by aqueous solution-phase exfoliation, is not well understood. Theoretically, a simple model based on the traditional DLVO (Derjaguin, Landau, Verwey, and Overbeek) theory has been proposed to describe: (i) the electrostatic repulsions between graphene sheets imparted by the adsorbed ionic surfactants and (ii) the strong van der Waals (vdW) attractions between the graphene sheets.[6,13] Several molecular dynamics (MD) simulation studies of the adsorption of the conventional linear surfactant, sodium dodecyl sulfate (SDS), on graphite, rather than graphene, have been reported.[35−37] Very recently, our group has investigated the dispersion stability of liquid-phase-exfoliated graphene in organic polar solvents using MD simulations and the kinetic theory of colloid aggregation.[38]

With all of the above in mind, in the present study, we carried out molecular simulations, theoretical modeling, and experimental measurements to elucidate several important aspects of aqueous solution-phase exfoliated graphene dispersions. First, we carried out molecular dynamics (MD) simulations to investigate the surface morphology of the ionic surfactant sodium cholate (SC) on a monolayer graphene sheet. The electrostatic potential around the graphene—SC assembly was calculated using the simulated charge density profile through the Poisson equation, as well as the theoretical Poisson—Boltzmann (PB) equation, to estimate the zeta potential around the assembly as a quantitative measure of colloid stability. The computed zeta potential was further compared to the experimental value obtained in the present study for a SC-stabilized graphene aqueous dispersion as well as to the value reported in the literature in the case of SDBS-stabilized graphene aqueous dispersions. To quantify the interactions between graphene sheets covered with cholate ions, we subsequently carried out a potential of mean force (PMF) calculation for two parallel graphene—SC assemblies, as a function of the intersheet separation, d, and compared the simulated results with those predicted using the traditional DLVO theory. On the basis of the simulated PMF profile, we then proposed a surfactant-stabilized metastable

structure for the exfoliated multilayer graphene sheets, which explains their turbostratic structure. Finally, to understand the kinetics of graphene aggregation, we combined the PMF results obtained using MD simulations with a kinetic theory of colloid aggregation to predict the time-dependent concentration and distribution of graphene with various thicknesses (or numbers of layers). We further decomposed each graphene layer type into subtypes, including the AB-stacked species and various turbostratic species. To study the dispersion stability of the graphene sheets in aqueous media, we prepared SC-stabilized graphene dispersions and monitored the graphene total mass concentration (including all graphene layer types) as a function of time based on the optical absorbance of the solution. Note that the initial layer number distribution of the prepared graphene sheets was characterized based on the experimentally obtained 2D Raman spectra. These experimental data were also used as inputs to our kinetic model to obtain the average collision area which is the only fitting parameter in the model.

2. METHODS

2.1. Simulation Method. Simulations of the self-assembly of sodium cholate on the graphene surface in aqueous solution were carried out using the GROMACS 4.0 software package.[39] Monolayer graphene was modeled as an infinite rigid sheet in the $x−y$ plane, similar to our recent simulations of graphene exfoliation in polar solvents.[38] The carbon atoms of graphene were treated as uncharged Lennard-Jones (LJ) spheres with $\sigma = 0.34$ nm and $\varepsilon = 0.223$ kJ/mol.[40] Water molecules and SC molecules were modeled using the SPC/E model[41] and the OPLS-AA force field,[42] respectively, similar to our recent simulations of SC-stabilized SWNT aqueous dispersions.[43] Bond lengths and angles in water molecules were constrained using the SETTLE algorithm,[44] while bond lengths in the cholate ions were constrained using the parallel version of the LINCS algorithm.[45] Lennard-Jones interactions were treated with a cutoff distance of 0.9 nm, with those between different atoms calculated using the standard geometric averaging rule implemented in the OPLS-AA force field.[42] Long-range electrostatic interactions were treated using the particle mesh Ewald (PME) summation method.[46,47] The velocity-rescaled Berendsen thermostat was implemented to maintain a constant system temperature of 298.15 K.[48] The semiisotropic Berendsen pressure coupling was applied,[49] where a pressure of 1 bar is coupled only in the z direction, such that the x and y dimensions of the simulation box can be fixed to match the size of the graphene sheet.

In the present study, 28 SC molecules were initially positioned near each side of a 56.6 nm^2 monolayer graphene sheet (i.e., a total of 56 SC molecules on both sides), which yields a surface coverage of $28/56.6 = 0.49$ molecule/nm^2 for each side of the sheet. As a point of reference, the experimental saturated SC surface coverage on a graphite surface, based on the Langmuir plot, was found to be around 0.38 molecule/nm^2.[50] A more rigorous simulation study involving various SC surface coverages to estimate the saturated SC surface coverage is in progress. For comparison with the case without SC, we also simulated a graphene sheet in water in the absence of SC. The energy of the simulated system was first minimized using the steepest-descent method.[39] The simulated system was then equilibrated for 250 ns, and data were collected for another 50 ns. The simulation was confirmed to have reached equilibrium within 250 ns by monitoring the SASAs (solvent accessible surface areas) of the cholate ions and graphene as a function of time (see Figure S1 in the Supporting Information). The simulated system size, including the total numbers of SC and water molecules, the total number of atoms, the size of the simulation box, and the total simulation time, are summarized in Table S1 in the Supporting Information.

The electrostatic potential around the graphene−SC assembly, $\Psi(z)$, along the z-axis of the simulation box, normal to the graphene surface, is related to the local charge density, $\rho(z)$, via the Poisson equation[51]

$$\frac{d^2\Psi(z)}{dz^2} = -\frac{\rho(z)}{\varepsilon\varepsilon_0} \qquad (1)$$

where $\varepsilon_0 = 8.85 \times 10^{-12}$ C/m·V is the vacuum dielectric permittivity and $\varepsilon = 78.5$ is the relative dielectric permittivity (or dielectric constant) of water at 25°. Note that the charge density, $\rho(z)$, results from the partial charges assigned to all the atoms in the system according to their force fields. In MD simulations, $\Psi(z)$ is calculated by integrating $\rho(z)$ twice along the z-axis numerically after dividing the simulation cell into many slabs along the z-axis. Details on the calculation of the electrostatic potential can be found in a recent review.[52]

To investigate the interactions between two parallel SC-covered graphene sheets, we calculated the potential of mean force (PMF) at various intersheet separations (along the z-axis of the simulation box), d, from $d_1 = 0.9$ nm to $d_2 = 3.4$ nm, with an increment of 0.05 nm. For $d \leq 0.9$ nm, the two graphene sheets cannot be compressed any further in our simulations due to the extremely long simulation time required for equilibration. For $d \geq 3.4$ nm, the average force exerted by the two graphene sheets is very close to zero. The PMF is calculated by numerically integrating, in a trapezoidal manner, the time-averaged force, $\langle F(d) \rangle$, exerted to separate the two graphene sheets at various d values. Specifically[53]

$$\text{PMF}(d) = \int_d^{d_2} \langle F(r) \rangle dr \qquad (2)$$

where r is the reaction coordinate which is the same as d. For a detailed discussion of the PMF calculations, the interested reader is referred to our recent publications.[38,43] Note that, in the PMF simulations, the x and y dimensions of the simulation box are larger than the lateral size of the graphene sheets (see Table S1 in the Supporting Information), to allow molecules which are confined between the two graphene sheets to escape from the intersheet gap. As a result, the graphene sheets in the PMF calculations are no longer infinite in the $x−y$ plane, and therefore, an isotropic pressure coupling was applied to carry out the PMF calculations. The equilibration of each simulation run was verified by the convergence of the cumulative average force as a function of the simulation time, as shown in Figure S2 in the Supporting Information.

2.2. Experimental Method. The bilayer-enriched SC-stabilized graphene dispersion, as reported in our recent work,[30] was used for the time-dependent graphene total mass concentration measurements carried out in the present study. The graphene solution was first decanted into three quartz cuvettes (to determine statistical errors), and the solution optical absorbance was then measured using a UV/visible spectrophotometer (Beckman Coulter DU800). The optical absorbance of the 2 wt % SC solution, which was used to prepare the graphene solution, was also measured and used as a reference. The correlation between the graphene total mass concentration and the optical absorbance per unit path length (A/l) was determined based on the Lambert−Beer law ($A = \alpha C_0 l$, where C_0 is the initial graphene total mass concentration measured using vacuum filtration, α the absorbance coefficient, and $l = 0.01$ m for the cuvette).[54] The graphene total mass concentration (in mg/L), $C(t)$, was monitored for two weeks based on the optical absorbance of the solution. The zeta potential of the graphene dispersion was measured using a Brookhaven ZetaPALS instrument at room temperature. The experimental procedures to prepare and characterize bilayer-enriched graphene dispersion using Stage-2 graphite intercalation compounds (GICs) are summarized in Section S1 in the Supporting Information.
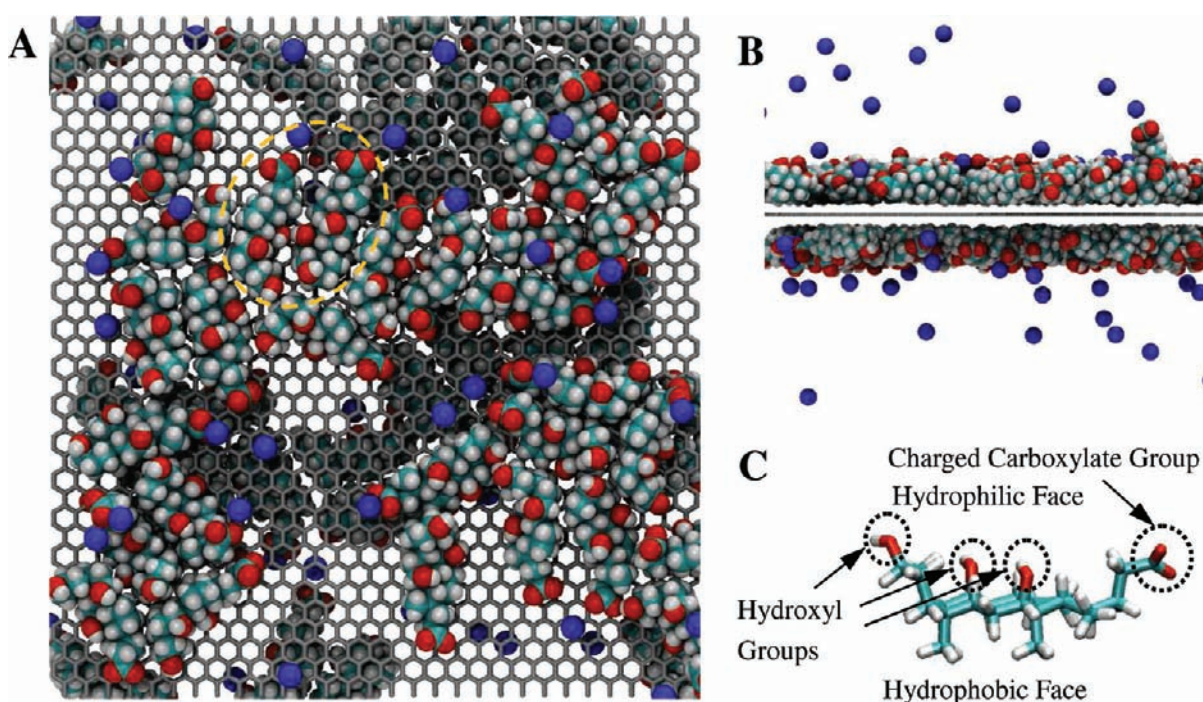
12812

dx.doi.org/10.1021/ja2048013 |*J. Am. Chem. Soc.* 2011, 133, 12810–12823

Figure 1. Representative postequilibrium simulation snapshots of SC-stabilized monolayer graphene: (A) top view, (B) side view, and (C) chemical structure of the cholate ion. Water molecules are not shown for clarity. Note that in (A) and (B) SC is shown in the volume-filled form, while the graphene sheet is shown in the stick form. The cholate ions at the back of the graphene sheet can also be visualized in a darker fashion. Note that the orange dashed ellipse highlights two side-by-side self-assembled SC molecules. Color code: red, oxygen; blue, sodium; light green, carbon; white, hydrogen; and silver, graphene carbon.

3. RESULTS AND DISCUSSION

3.1. Surface Morphology of the Monolayer Graphene−SC Assembly.

Representative postequilibrium simulation snapshots of a monolayer graphene sheet covered with cholate ions are shown in Figures 1A and 1B. Similar to the surface self-assembly structure of cholate ions on a SWNT,[43] the cholate ions adsorb parallel to the graphene surface, with their hydrophilic faces (having oxygen atoms shown as red spheres in Figure 1C) located farther away from the hydrophobic graphene surface and, consequently, with their hydrophobic faces facing the hydrophobic graphene surface. This finding is consistent with the speculation that the planar SC molecules form a stable charged encapsulation layer on each side of the suspended graphene sheets.[15] This organization tends to maximize the contact between the hydrophobic faces of the cholate ions and the graphene surface and is driven by the hydrophobic effect.[55] Another interesting feature in the front-view simulation snapshot in Figure 1A is that, instead of distributing uniformly on the graphene surface, the adsorbed cholate ions prefer to self-assemble side-by-side, also due to the hydrophobic effect.[55] Note that this side-by-side SC organization (highlighted by the orange dashed ellipse) tends to minimize contact between the hydrophobic faces of the cholate ions and water. This side-by-side SC self-assembly is also facilitated by the condensation (or binding) of positively charged sodium counterions onto single, or multiple, negatively charged cholate ions (typically, onto the charged carboxylate groups, as shown in Figures 1A and 1B). Indeed, the sodium counterion condensation shields the electrostatic repulsions between the charged carboxylate groups and effectively brings them closer to each other.

The organization of SC on the graphene surface is further quantified in the density profiles of the water molecules, the cholate ions, and the sodium counterions along the z-axis (normal to the graphene sheet, see Figure 2A). The density profile of the cholate ions (red line in Figure 2A) indicates that they prefer to distribute in a very compact manner within 1 nm on the graphene surface (where the density profile decays to zero beyond $z = \pm 1$ nm). Taking into account the thickness of the graphene sheet (≈ 0.4 nm), the result in Figure 2A shows that cholate ions aggregate as a compact layer with a thickness of 1 nm − 0.4 nm/2 = 0.8 nm, consistent with their molecular thickness of around 0.7 nm. The sodium counterion condensation effects can also be observed in Figure 2A, where the largest peak of the density profile of the sodium counterions around the graphene sheet (green line, $z = \pm 0.75$ nm) is closely located to the largest peak of the cholate ions (red line, $z = \pm 0.5$ nm), reflecting the strong electrostatic attractions between these oppositely charged ions. The difference between these two peaks, 0.75 − 0.5 = 0.25 nm, is consistent with the vdW radius of 0.21 nm of a sodium counterion. The unbound sodium counterions diffuse away from the graphene−SC assembly to the bulk region (with a bulk concentration of around 1.7 kg/m^3, measured at the z-boundary of the simulation box). Water ordering on the hydrophobic graphene surface is well-known in the literature,[56] which is demonstrated by fluctuations (with sharp peaks representing the hydration layers) in the density profile near the graphene surface (the blue dashed line in Figure 2A corresponding to the water density profile without SC). Interestingly, in the presence of the adsorbed cholate ions (the blue line in Figure 2A), the first and the second hydration layers, corresponding to the two closest peaks in the density profile at each side of the graphene sheet, are suppressed (about 50% for the first hydration layer, with the second hydration layer no longer
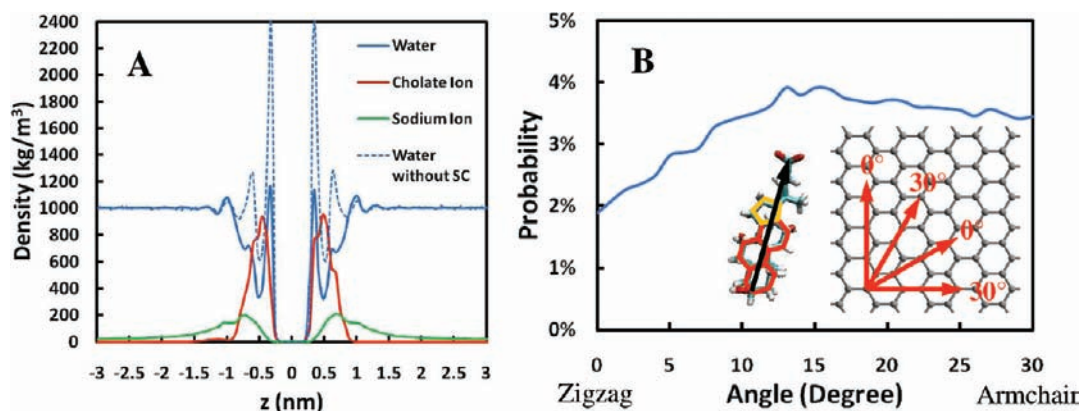
Figure 2. (A) Simulated density profiles of water molecules, cholate ions, and sodium couterions along the z-axis normal to the monolayer graphene. Note that the z-axis was shifted so that the graphene sheet is located at $z = 0$. The water density profile for the simulation of graphene in water, without SC, is shown as the blue dashed line for comparison. Note also that the density of the sodium counterions was amplified 10 times for clarity. (B) Simulated distribution profile of the angles (with a 1° interval) between the principal axis of the cholate ions and the zigzag axis (0°) of graphene. In the SC molecular structure shown, the solid black line connecting the carbon atom in the carboxylate group with the carbon atom at the end of the steroid ring defines the principal axis of the cholate ion. Furthermore, the three red hexagonal rings represent the "armchair-like" cyclohexane rings in the cholate ion, while the orange pentagonal ring represents the cyclopentane ring in the cholate ion.

visible) compared to the case without SC. It is noteworthy that the third hydration layer is not affected at all because the cholate ions do not extend beyond the location of the second hydration layer.

As discussed earlier, the cholate ions prefer to adsorb parallel to each other on the graphene surface. However, the precise orientations of the cholate ions with respect to the zigzag or armchair axes of graphene still need to be determined. For this purpose, we calculated the distribution of the angles (with a 1° interval) between the principal axis of the cholate ions (defined in Figure 2B) and the zigzag axis of graphene. As shown in Figure 2B, the cholate ions orient quite uniformly on the graphene sheet (the probabilities range from 2% to 4%). In other words, the cholate ions do not exhibit a large tendency to orient along the zigzag (0°) or the armchair (30°) axes of graphene. However, they do exhibit a small tendency to orient in between the two axes (the largest peak in the angle distribution profile corresponds to 15°). Comparing the angle distribution near 0° and 30°, one can conclude that the cholate ions have a slightly greater tendency to orient along the armchair axis than along the zigzag axis. This angular orientation is probably due to the fact that the three cyclohexane rings in the cholate ion (see Figure 2B) form an "armchair-like" structure (with respect to its principal axis), which favors the orientation along the armchair axis of graphene. Furthermore, it is highly possible that the cyclopentane ring in the cholate ion (see Figure 2B) disfavors such an orientation and shifts the peak to 15°.

Finally, to confirm that the simulated surface coverage of cholate ions agrees with the experimental saturated value, we calculated the density of a monolayer graphene–SC assembly, ρ_{GRA-SC}, by averaging the total density profile along the z-axis (including those corresponding to the graphene sheet, ρ_{GRA}, the cholate ions, $\rho_{cholate}$, the sodium counterions, ρ_{sodium}, and the bound hydration shell of water molecules, ρ_{water}) from $z_1 = -1.5$ to $z_2 = 1.5$ nm (see Figure 2A), as follows

$$\rho_{GRA-SC} = \frac{1}{z_2 - z_1} \int_{z_1}^{z_2} (\rho_{GRA} + \rho_{cholate} + \rho_{sodium} + \rho_{water}) dz \tag{3}$$

The bound hydration shell of water molecules is defined to be located along the z-axis from $z_1 = -1.5$ to $z_2 = 1.5$ nm. Note that $z = \pm 1.5$ nm corresponds to the position where the water density profile initially reaches its bulk value (namely, beyond $z = \pm 1.5$ nm, the water density fluctuations begin to disappear, see Figure 2A). Consistent with the buoyant density of the monolayer graphene–SC assembly measured experimentally (1.16 g/mL),[15] the simulated value of ρ_{GRA-SC} is equal to 1.18 g/mL. Note that the experimentally estimated saturated surface coverage of SC on graphene, obtained by fitting the buoyant densities of the graphene–SC assemblies comprising various graphene layers to a simple geometric model (1.35 molecules/nm²),[15] is about two times larger than our simulated value (0.49 molecules/nm²). For comparison, the experimental saturated SC surface coverage on the graphite surface estimated based on a Langmuir plot is approximately equal to 0.38 molecule/nm²,[50] which is significantly closer to our simulated value. In the simulation, the cholate ions only partially cover the graphene surface with an estimated fraction of 60% of the graphene surface area, based on the surface area of 1.5 nm × 0.8 nm = 1.2 nm² occupied by a cholate ion. On the other hand, the experimentally reported value is 94%, based on a surface area of 0.7 nm² occupied by a cholate ion,[15] which is smaller than the value that we estimated. We believe that this discrepancy is probably due to the limitation of the simple geometric model proposed by Green et al.,[15] which is based on the assumption that there are no molecules confined between multilayer graphene sheets (see discussion in Section 3.4).

Interestingly, visual analysis of Figure 1A suggests that the cholate ions adsorbed on the two sides of the graphene sheet overlap very little with each other, with a visually estimated overlap area of 25% over the graphene surface area. Note that the theoretical minimum overlap area should be 2 × 60% − 100% = 20% over the graphene surface area. On the other hand, the overlap area for cholate ions that are independently distributed on each side of the graphene sheet should be 60% × 60% = 36% over the graphene surface area. This difference may be due to the correlation between the cholate ions on each side of the graphene sheet resulting from electrostatic repulsions between the negatively charged cholate ions, which favors a smaller overlap area.
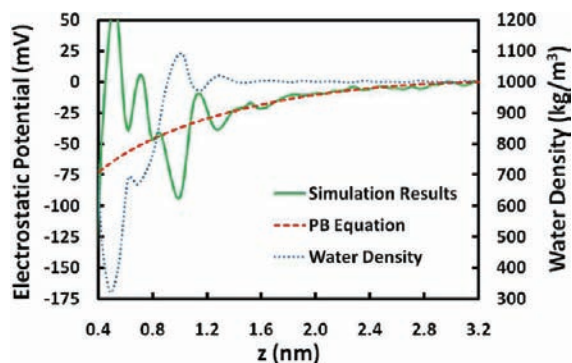
Figure 3. Simulated electrostatic potential around the graphene–SC assembly as a function of z, compared to that predicted based on the traditional Poisson–Boltzmann (PB). The water density profile is shown for comparison purposes.

3.2. Electrostatic Potential around the Monolayer Graphene–SC Assembly. The simulated electrostatic potential, $\Psi(z)$, around the graphene–SC assembly, along the positive z-axis, is shown in Figure 3. For comparison, we predicted the electrostatic potential based on the traditional Poisson–Boltzmann (PB) equation. It is quite reasonable to assume that the cholate ions are bound tightly onto the graphene surface and do not contribute to the solution ionic strength since the simulated concentration of the cholate ions in the bulk solution is negligible compared to that of the sodium counterions. This results in[51]

$$\frac{d^2\Psi(z)}{dz^2} = -\frac{\rho_\infty}{\varepsilon\varepsilon_0}\exp\left(-\frac{e\Psi(z)}{k_B T}\right) \tag{4}$$

where $\rho_\infty = 7.12 \times 10^6$ C/m^3 is the bulk charge density of the sodium counterions based on their bulk concentration of 1.7 kg/m^3 (obtained in Section 3.1); $e = 1.60 \times 10^{-19}$ C is the electronic charge; $k_B = 1.38 \times 10^{-23}$ J/K is the Boltzmann constant; and $T = 298.15$ K is the simulated room absolute temperature. By solving eq 4 at the simulated boundary conditions, where $\Psi = 0$ and $d\Psi/dz = 0$ at the z-boundary of the simulation box, we obtain[51]

$$\Psi(z) = \frac{2k_B T}{e}\ln\left(\cos\frac{\kappa z}{\sqrt{2}}\right) \tag{5}$$

where $\kappa = [(e\rho_\infty)/(\varepsilon\varepsilon_0 k_B T)]^{1/2}$ is the inverse of the Debye–Hückel (DH) screening length (or the double-layer thickness). Note that the result in eq 5 is different from that obtained using the Goüy-Chapman theory,[51] which yields the solution to the PB equation at a different boundary condition where $\Psi(z \rightarrow \infty) = 0$. Furthermore, note that due to the periodic boundary conditions imposed by the simulation box the predicted $\Psi(z)$ profile was shifted such that $\Psi(z_{max}) = 0$, where $z_{max} = \pm 3.2$ nm is the boundary of the simulation box along the z-axis, to allow comparison with the simulated $\Psi(z)$ profile.

As shown in Figure 3, $\Psi(z)$ predicted using the PB equation (the red dashed line) is always negative due to the negatively charged cholate ions adsorbed on the graphene surface. In the far-field continuous aqueous media region away from the graphene surface ($z \geq$ the Debye–Hückel screening length, $1/\kappa = 1.6$ nm), the simulated $\Psi(z)$ (the green line) agrees very well with $\Psi(z)$ predicted using the PB equation, whose magnitude decays in an exponential manner due to the screening effects of

the positively charged sodium counterions. However, in the near-field region close to the graphene surface ($z \leq 1/\kappa = 1.6$ nm), the simulated $\Psi(z)$ fluctuates significantly, unlike the smooth curve obtained using the PB equation for $z \leq 1.6$ nm. By comparing the fluctuations in the simulated water density profile (the blue dotted line) and in the simulated $\Psi(z)$, one can observe a strong negative correlation between the simulated water density and $\Psi(z)$ profiles (i.e., when there is a peak in $\Psi(z)$, there is a valley in the water density profile, and vice versa). This results from the algorithm used to divide the z-dimension of the simulation box into small slabs (0.05 nm in thickness) to determine the water density profile and $\Psi(z)$. For water molecules which are highly ordered, there is a nonuniform distribution of mass inside of each slab. The slabs in which more oxygen atoms (heavier than hydrogen atoms) are located will possess higher local densities, corresponding to the peaks in the water density profile. Similarly, the hydrogen atoms contribute to the valleys in the water density profile. By drawing the analogy between mass and charge and taking into account the relations between $\Psi(z)$ and the local charge density, $\rho(z)$, through eq 1, one can observe that the negatively charged oxygen atoms contribute to the valleys in $\Psi(z)$, while the positively charged hydrogen atoms contribute to the peaks in $\Psi(z)$. We can therefore conclude that the fluctuations observed in the simulated $\Psi(z)$ profile result from the ordering of water molecules near the graphene surface, a discrete molecular event that cannot be reproduced by the traditional PB equation where water is treated as a continuum.[57]

To determine the zeta potential, ζ, of the graphene–SC assembly, one needs to determine the location of the surface of shear at which ζ is defined.[58] Considering the surface of the graphene–SC assembly as a negatively charged wall due to the adsorbed cholate ions, an appropriate definition of the surface of shear is the outer surface of the cholate ions, where the density profile of the cholate ions approaches zero at $z = 1$ nm (see Figure 2A). The simulated ζ is equal to -93 mV at $z = 1$ nm, which is about two times larger in magnitude than the ζ value predicted using the PB equation (-37 mV). For comparison, the zeta potential for SC-stabilized graphene measured in the present study is -45 ± 5 mV based on five different measurements, which is similar to the reported value of -50 mV for SDBS-stabilized graphene.[13] On the basis of the simulated ζ value, we can conclude, not surprisingly perhaps, that the traditional PB equation is not able to accurately predict the near-field properties, including ζ, of graphene–SC assemblies. It is also quite clear that the commonly used Debye–Hückel (DH) approximation to the PB equation (which should be appropriate when $|\zeta| \ll k_B T/e = 25.7$ mV for monovalent ions)[51] cannot be used in the case of graphene–SC assemblies for which $\zeta = -93$ mV. Note that charged surfactants adsorbed on the graphene surface may facilitate the adsorption of oppositely charged reactants present in the solution.[31] As a result, the impact of the graphene surface charge resulting from charged surfactant adsorption is also an important factor in determining the functionalization selectivity of graphene, in addition to the surfactant surface coverage. Moreover, specific binding (e.g., hydrophobic bonding, hydrogen bonding, or ring stacking) between surfactants and reactants should also be taken into consideration in determining the functionalization selectivity of graphene.

3.3. Interactions between Two Graphene–SC Assemblies. The interactions between two parallel graphene–SC assemblies were quantified using the potential of mean force (PMF) between them, as a function of the intersheet separation, d, as
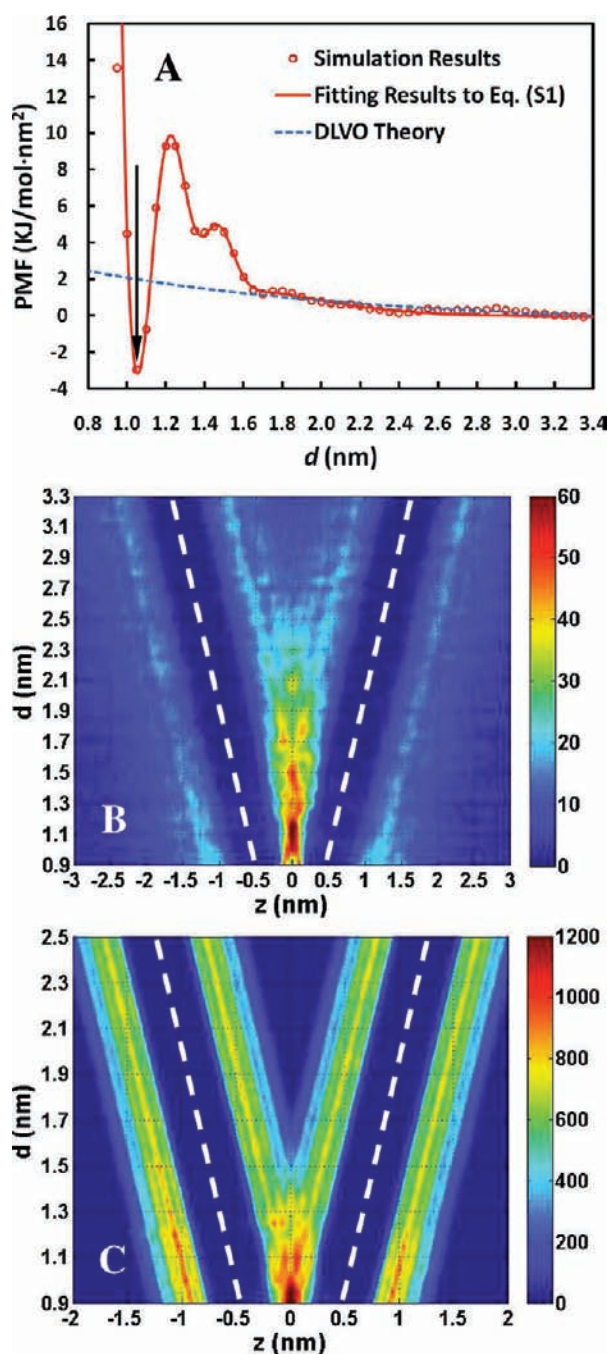
12815

dx.doi.org/10.1021/ja2048013 |*J. Am. Chem. Soc.* 2011, 133, 12810–12823

Figure 4. (A) Simulated potential of mean force (PMF) between two parallel graphene−SC assemblies as a function of the intersheet separation, d. The fitting results to the simulated PMF data (shown in red circles) using eq S1 in Section S2 (Supporting Information) correspond to the red solid line. The predicted electrostatic repulsive potential using the DLVO theory corresponds to the blue dashed line and is shown for comparison. Note that the arrow shows the position of the local minimum at $d = 1.05$ nm in the PMF profile. (B) and (C) The contour plots of the density (in units of kg/m^3) profiles of: (B) the sodium counterions and (C) the cholate ions, both along the z-axis, as a function of d. The red-color regions illustrate the existence of a sodium ion wall in (B) and a single layer of cholate ions in (C), both being confined by the two graphene sheets. Note that the density increases as the color changes gradually from blue to red. Note also that the white dashed lines denote the z-axis positions of the graphene sheets, as a function of d.

shown in Figure 4A. The simulated PMF profile (the red circles) exhibits a primary, long-range repulsive potential energy barrier possessing a maximum of around 10 kJ per mole and per unit area (in nm^2) of the simulated graphene sheet, extending from $d = 1.2$ to 3.4 nm. The PMF profile in Figure 4A also exhibits a local energy minimum of -3 kJ/mol·nm^2 at $d = 1.05$ nm. As d decreases further from 1.05 to 0.9 nm, the PMF profile goes up sharply until the point where the two graphene sheets cannot be compressed any further in our simulations due to the extremely long simulation time required for equilibration.

From $d = 2.2$ to 3.4 nm, the onset of the repulsive potential energy barrier in the PMF profile is due to the long-range electrostatic repulsion between the two parallel graphene−SC assemblies, which behave as two parallel, negatively charged plates, mediated by the positively charged sodium counterions. This contribution to the potential energy barrier has been widely recognized to result from the electrostatic contribution which appears in the traditional DLVO theory.[51] Considering that the DH approximation for low potentials is not appropriate for the case considered here, the repulsive electrostatic potential per unit area in the DLVO theory should be calculated under the weak-overlap approximation as follows[51]

$$U(d) = \frac{64 k_B T \rho_\infty \gamma^2}{e \kappa} \exp(-\kappa d) \qquad (6)$$

where $\gamma = \tanh[(e\Psi_0)/(4k_B T)]$, and the surface potential Ψ_0 can be calculated using the Grahame equation,[51] where $\Psi_0 = -[(k_B T)/e]\ln[((e\sigma^2)/(2\varepsilon\varepsilon_0 k_B T \rho_\infty)) + 1] = -83$ mV, and the surface charge density resulting from the bound cholate ions, $\sigma = -0.08$ C/m^2. Note that this value of Ψ_0 is slightly different from that of the simulated zeta potential $\zeta = -93$ mV. This is due to the fact that the ζ value was obtained from the monolayer graphene simulation rather than from the bilayer graphene simulation used here. In addition, note that the calculated $U(d)$ profile in eq 6 was shifted such that $U(d_{max}) = 0$, where $d_{max} = 3.4$ nm is the largest intersheet separation, to allow comparison with the simulated PMF profile.

As shown in Figure 4A, the simulated repulsive electrostatic potential and that predicted using the DLVO theory (eq 6, blue dashed line) agree very well in the far-field continuous aqueous media region ($d \geq 1.6$ nm). In addition, the DLVO contribution to the primary potential energy barrier is quite small, which is somewhat unexpected based on recent theoretical reports,[6,13] due to the fact that only the electrostatic effect was considered in these reports. As expected, the DLVO theory prediction deviates significantly from the simulated PMF in the near-field region ($d \leq 1.6$ nm) due to the neglect of the molecularity of the directly contacted cholate ions, sodium counterions, and water molecules in the DLVO theory. As will be discussed in Section 3.4, the major contribution to the energy barrier inhibiting graphene aggregation is the steric repulsion exerted by the sodium counter-ion wall and the single layer of cholate ions which are confined between the two graphene sheets. This finding is consistent with our recent simulation studies on: (i) surfactant-stabilized SWNTs[43] and (ii) liquid-phase-exfoliated graphene in polar solvents.[38] Note that, typically, only long-chain polymers are presumed theoretically to contribute to the steric repulsion between colloidally dispersed particles such as graphene.[59] On the other hand, we demonstrate here that small surfactant molecules like SC can also contribute greatly to the steric repulsion, as a result of their high binding affinities to the graphene sheet.
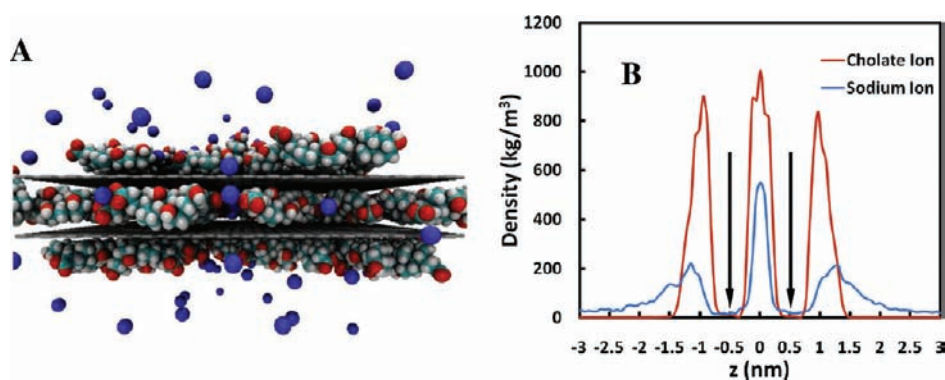
12816

dx.doi.org/10.1021/ja2048013 |*J. Am. Chem. Soc.* 2011, 133, 12810–12823

Figure 5. (A) Postequilibrium simulation snapshot of the metastable bilayer graphene—SC assembly at an intersheet separation of $d = 1.05$ nm, showing a single layer of cholate ions and a sodium counterion wall confined between the two graphene sheets. Water molecules are not shown for clarity. The color code is the same as in Figure 1. (B) The simulated density profiles of the cholate ions and the sodium counterions along the z-axis, showing a single layer of cholate ions and a sodium counterion wall (both peaked at $z = 0$ nm) being confined between the two graphene sheets located at $d = 1.05$ nm (or at $z = \pm 0.525$ nm, as pointed out by the two arrows). Note that the other four peaks (two peaked at $z = \pm 0.9$ nm and two peaked at $z = \pm 1.15$ nm) show the adsorbed cholate ions and sodium counterions at the outer surfaces of the two graphene sheets.

For $d \leq 2.2$ nm, the onset of sodium counterion-induced steric repulsion[51,60,61] between two graphene—SC assemblies further enhances the potential energy barrier (see Figure 4A), a phenomenon that has also been observed in the case of SWNTs stabilized by SC.[43] In fact, the existence of a concentrated sodium counterion wall for $d \leq 2.2$ nm is shown in Figure 4B, which illustrates the simulated contour plot of the density profile of the sodium counterions along the z-axis of the simulation box normal to the graphene surface, as a function of d. For $d \leq 1.5$ nm, the cholate ions adsorbed on the graphene surfaces begin to establish contact with each other (see Figure 4C for a contour plot of their density profile), which results in direct interactions between them. These interactions lead to the oscillatory behavior of the PMF profile (for $d \leq 1.5$ nm in Figure 4A), which has been widely recognized to result from the interplay between the van der Waals (vdW) attraction and the hard-core steric repulsion between materials.[62] This oscillatory behavior, reflecting the molecularity of all condensed phases in nature, has been extensively studied experimentally in the case of liquids confined to molecular separations by two approaching smooth mica surfaces.[63−65]

Although the cholate ions adsorbed on the graphene surfaces begin to contact each other at $d \leq 1.5$ nm, the partially covered graphene surfaces allow the cholate ions to exchange between them to efficiently cover the empty areas on both surfaces (the merging of the two green bands in Figure 4C) without incurring steric penalties (from $d = 1.2$ to 1.05 nm in Figure 4A). The density of the cholate ions in the intersheet gap increases from $d = 1.2$ to 1.05 nm (from green to orange in Figure 4C). As the intersheet separation decreases from 1.05 to 0.9 nm, the density of the cholate ions in the intersheet gap further increases (from orange to red in Figure 4C), and as a result, a single layer of cholate ions is confined and exerts a strong steric repulsive force between the two graphene sheets (from $d = 1.05$ to 0.9 nm in Figure 4A). Accordingly, the simulated oscillatory PMF profile as the intersheet separation decreases can be rationalized as follows: (i) the cholate ions begin to contact each other and exchange between the two graphene surfaces from $d = 1.5$ to 1.2 nm; (ii) the intersheet gap begins to accommodate only a single layer of cholate ions from $d = 1.2$ to 1.05 nm; and (iii) the two graphene sheets begin to compress the single layer of cholate ions

for $d \leq 1.05$ nm. Note that in Figure 4C the density of the cholate ions on the outer surface of the bilayer graphene—SC assembly (the left-most and the right-most bands) increases (from green to orange) slightly for $d \leq 1.5$ nm, which suggests that some of the cholate ions, originally confined between the two sheets, desorb from (or are squeezed out of) the intersheet gap and then readsorb onto the outer surface.

3.4. Metastable Bilayer Graphene and the Turbostratic Layering Structure. Most interestingly, as a result of the local energy minimum at $d = 1.05$ nm (see Figure 4A), the bilayer graphene—SC assembly, featuring a single layer of cholate ions and a sodium-ion wall confined between the two graphene sheets (see Figure 5A), is metastable in the aqueous solution. Note that our proposed "sandwich-like" bilayer graphene structure is referred to as "metastable" because the most stable structure of bilayer graphene should occur when the two graphene sheets contact each other directly. As reported in other simulation studies,[38,56] the two graphene sheets establish the global energy minimum at $d = 0.35$ nm, resulting from the balance between the intersheet vdW attractions and steric repulsions. A more detailed characterization of the bilayer graphene structure shown in Figure 5A can be obtained by examining the simulated density profile of the cholate ions and the sodium counterions around two graphene sheets at the local energy minimum where $d = 1.05$ nm, as shown in Figure 5B. The high cholate ion and sodium counterion densities at the intersheet gap greatly hinder the aggregation of the two graphene sheets by counterbalancing the intersheet vdW attraction with the SC-induced steric repulsion. When such steric repulsion precisely counterbalances the intersheet vdW attraction, the two graphene sheets are locked in the normal direction. Moreover, due to the relatively short-ranged vdW attraction between two graphene sheets (we recently showed that it decays to almost zero when $d > 1.0$ nm, see Figure 2 of ref 38), at $d = 1.05$ nm, the two graphene sheets should be able to translate freely parallel to each other. As a result, the layering structure of the two parallel graphene sheets is turbostratic even before they are able to reaggregate to form AB-stacked bilayers by completely squeezing out the confined cholate ions and sodium counterions. The local minimum in the PMF profile induced by the confined solvent molecules was also observed in the case of liquid-phase-exfoliated graphene in
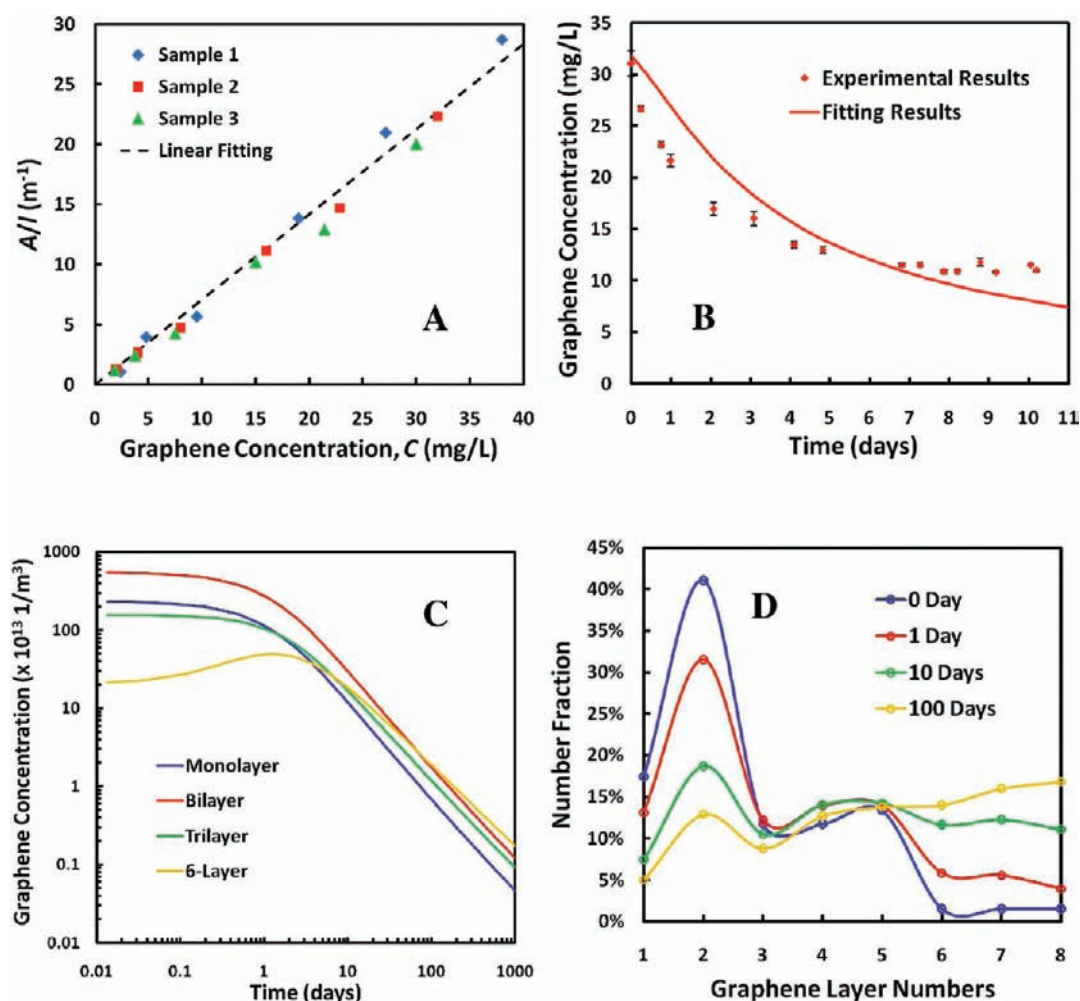
Figure 6. (A) Measured optical absorbance (at 660 nm wavelength) per unit path length (A/l) as a function of the total graphene mass concentration, C. Note that three different samples (corresponding to the red, blue, and green symbols) were prepared using the same procedure. (B) Time-dependent graphene total mass concentration, $C(t)$, as a function of time. The red line denotes the numerical fitting results from eqs S1—S6 in Section S2 (Supporting Information). The errors in the experimental results (the black markers) were obtained from the standard deviations in the optical absorbance of the three cuvette samples. (C) Predicted time-dependent number concentrations of graphene with various layer numbers, $N_i(t)$, as a function of time. Note that six-layer graphene is used to represent thicker multilayer graphene. (D) Predicted distributions of graphene layer numbers as a function of time. Note that the circles are the actual values, and each line that smoothly connects the circles is just a guide to the eye.

polar solvents, as shown in our recent simulation study.[38] However, the difference between the two cases may be summarized as follows: (i) in the polar solvent case, the steric repulsion is induced by the last confined layer of solvent molecules before desorption from the intersheet gap, due to the stronger affinity between the solvent molecules and graphene; (ii) in the surfactant case, the steric repulsion is induced by the last confined layer of cholate ions and sodium counterions, rather than by the solvent (water) molecules, due to that fact that water molecules do not have strong affinity for graphene, while the cholate ions do. In addition, the positively charged sodium counterions are able to associate electrostatically with the negatively charged cholate ions.

For multilayer graphene, the Bernal AB-stacking found in natural graphite is the most energetically favorable structure. Nevertheless, turbostratic non-AB-stacking graphene sheets have been observed in solution-phase samples after DGU.[15] Here, we found that the existence of a single layer of confined cholate ions and sodium counterions not only efficiently extends the aggregation

process as mentioned earlier but also greatly disorders the AB-stacking structure of the multilayer graphene sheets. Specifically, we observe that the surfactant, or the polar solvent, acts like a double-edged sword: it prevents the reaggregation of both monolayer and multilayer graphene sheets, but it also prevents the reaggregation of two monolayer graphene sheets into one bilayer graphene sheet (as well as into AB-stacked bilayer graphene). When the surfactants or the polar solvents eventually completely desorb from the intersheet gaps, one would expect that the original bilayer graphene has already reaggregated with other graphene sheets to form much thicker multilayer graphene sheets (although they have become AB-stacked, they are too thick for practical applications). In other words, surfactants or polar solvents are not able to selectively stabilize monolayer, bilayer, or trilayer graphene sheets when they form initially as part of the exfoliation process (see Section 3.5 for additional discussion). Therefore, we may conclude that the simulated metastable bilayer graphene structure can explain well the experimental observation of large populations of non-AB-stacked bilayer and trilayer graphene.[15] Our explanation is also

consistent with the experimental speculations that this source of disorder may be induced during strong horn ultrasonication, as well from reaggregation of previously exfoliated graphene sheets covered with surfactants.[15]

To further confirm the proposed metastable bilayer graphene structure, we calculated the density for the bilayer graphene–SC assembly at $d = 1.05$ nm (see Figure 5A). On the basis of the method (eq 3) discussed in Section 3.1 for monolayer graphene, the calculated density for the bilayer graphene–SC assembly is equal to 1.25 g/mL, consistent with the buoyant density of bilayer graphene measured experimentally (1.23 g/mL).[15] This further suggests that: (i) the bilayer graphene dispersions obtained by Green et al. using the DGU method may be composed of the metastable, "sandwich-like" graphene proposed here and (ii) DGU may not be a viable approach to exfoliate graphite to yield AB-stacked graphene, probably due to the long-time centrifugation which concentrates graphene near the isopycnic point such that the reaggregation is accelerated.

3.5. Experimental and Predicted Total Graphene Dispersion Stability. As shown in Figure 6A, the correlation between the graphene total mass concentrations and the optical absorbance per unit path length (A/l) was calibrated based on the Lambert–Beer law ($A = \alpha C_0 l$). The linear regression yielded $\alpha = 0.71$ L/mg·m (± 0.03 L/mg·m from the mean square error of the regression). The time-dependent graphene total mass concentration, $C(t)$, monitored based on the solution optical absorbance, is shown in Figure 6B. The concentration decreases from an initial value of around 31 mg/L to a relatively stable value of around 11 mg/L within a week. The concentration vs time profile in Figure 6B exhibits an exponential decay, similar to that observed in the case of graphene exfoliated in polar organic solvents,[8] with a loss of around 65% in the graphene concentration. The initial graphene layer number distribution is shown in Figure 6D (the blue line at day zero), exhibiting a bilayer-enriched graphene solution. To connect the initial graphene layer number distribution to the initial graphene number concentrations, N_{i0}, we took into account the initial graphene total mass concentration ($C_0 = 31$ mg/L) and assumed that all the graphene sheets have the same area of $1 \mu m^2$, which corresponds to the average value observed by transmission electron microscopy (TEM). Therefore, the weight of monolayer graphene (4.7×10^5 mg/mol) could be obtained. Subsequently, the weight of other multilayer graphene could be obtained by multiplying the weight of monolayer graphene by the layer numbers.

The MD simulation results presented so far have provided a thermodynamic description of the dispersion stability of solution-phase exfoliated graphene. However, for practical purposes, the aggregation kinetics of graphene must be investigated to quantify the lifetime and the quality of these dispersions. Recently, we developed a theoretical model that combines the PMF results from MD simulations with the theory of slow colloid coagulation.[38,66] In our study of graphene dispersions in organic polar solvents, this model was used to correlate the simulated PMF results[38] with the time-dependent graphene layer number distribution observed in actual experiments.[8] In the present study of SC-stabilized graphene dispersions, we generalize this model to correlate the simulated PMF results with the time-dependent graphene concentration observed in our experiments. The kinetic theory of graphene aggregation is discussed in detail in Section S2 in the Supporting Information.

To utilize the kinetic model described above to calculate the time-dependent number concentration of various graphene layer types, $N_i(t)$, it is first necessary to estimate the value of A_C. The collision area, A_C, can be obtained by least-squares fitting the predicted time-dependent graphene total number concentration, $N_{total}(t)$, to the measured graphene total mass concentration, $C(t)$. Specifically, $N_{total}(t)$ can be calculated as the sum over the time-dependent concentrations of all the i-layer graphene sheets, that is

$$N_{total}(t) = \sum_{i=1}^{M} N_i(t) \tag{7}$$

We can relate the various components of $N_{total}(t)$ (in $1/m^3$) with $C(t)$ (in mg/L) using the assumption that all the graphene sheets have the same area of $1 \mu m^2$. The nonlinear minimization algorithm for the least-squares fitting was carried out utilizing the interior-reflective Newton method subroutine in the MATLAB numerical library. After incorporating eq 7 into eqs S1–S6 in Section S2 (Supporting Information), as shown in the fitting curve in Figure 6B, we deduced the best-fit average collision area, $A_C = 1.57$ nm^2, and the rate constant of aggregation, $k = 7.54 \times 10^{-22}$ m^3/s. The total least-squares error of the fitting is 173.2 mg^2/L^2, which corresponds to a significant error of 3.2 mg/L (around 10% for an initial concentration of 31 mg/L and 30% for a steady-state concentration of 11 mg/L) for each fitted concentration value, using solely the single fitted parameter, A_C. A more complex model with additional fitting parameters is probably required to replace this error but is outside the scope of this paper.

Next, using the deduced A_C value of 1.57 nm^2, we predict the time-dependent graphene number concentration of various layer types, as shown in Figure 6C. Using a similar procedure, we predicted the time-dependent graphene layer number distributions in Figure 6D. In Figure 6C, all the monolayer, bilayer, and trilayer graphene concentrations decrease with time in an exponential manner. If one defines the lifetime of solution-phase graphene as the time required for the concentration of monolayer or bilayer graphene sheets to be reduced by $1/e$, the lifetime of graphene is only about 1 day. However, in the case of trilayer graphene, the lifetime is about 2 days, as a result of having both monolayer and bilayer graphene as sources. Moreover, in the case of thicker multilayer graphene, such as six-layer graphene, its number concentration actually increases to a maximum in about 2 days and then decreases, with a lifetime which is longer than 10 days (see Figure 6C). This behavior results primarily from the reaggregation of monolayer and thinner multilayer graphene, which in general shifts the layer number distribution in the direction of thicker layers as time evolves, as shown in Figure 6D. Although the number concentration of bilayer graphene decreases by $1/e$ in about 1 day (see Figure 6C), its layer number distribution is still higher ($\geq 18\%$) compared to other layer types up to 10 days (see Figure 6D), which may be attributed to the initial bilayer-enriched graphene solution from Stage-2 GICs.

3.6. AB-Stacked and Turbostratic Graphene Dispersion Stability. As discussed in Section 3.4, for the SC-stabilized graphene dispersions considered here, the reaggregated graphene tends to be turbostratic with one additional SC monolayer sandwiched between the two graphene sheets. As a result, the reaggregated graphene sheets are intrinsically different from the as-prepared AB-stacked graphene. It then follows that each layer-number type graphene should consist of multiple subtypes of graphene, including the as-prepared
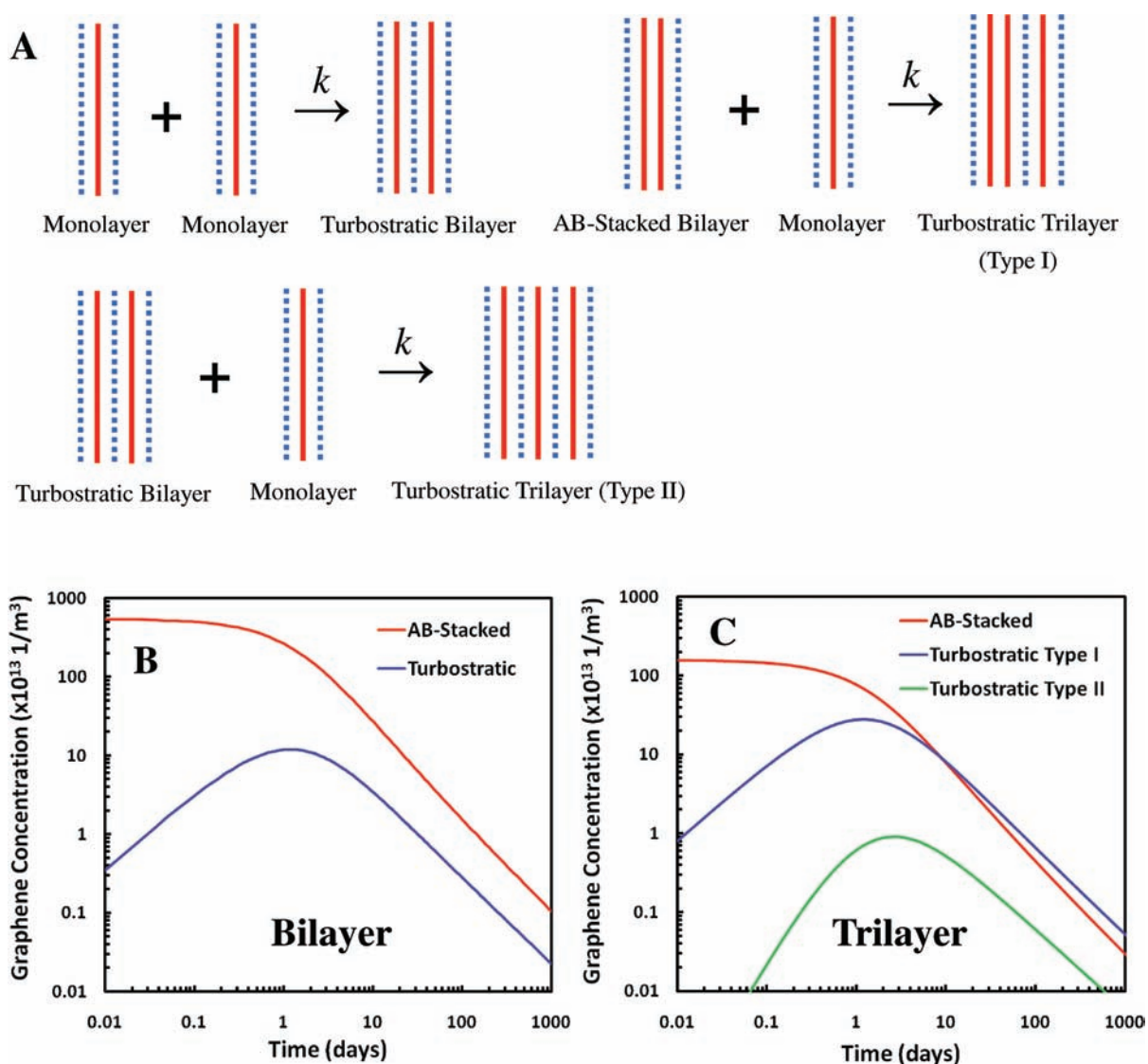
12819

dx.doi.org/10.1021/ja2048013 |*J. Am. Chem. Soc.* 2011, 133, 12810–12823

Figure 7. (A) Reaggregation mechanisms of turbostratic bilayer and trilayer graphene. The turbostratic bilayer graphene results from the reaggregation of two monolayer graphene sheets. The turbostratic trilayer graphene results from the reaggregation of one AB-stacked bilayer graphene and one monolayer graphene (type I) or from the reaggregation of one turbostratic bilayer graphene and one monolayer graphene (type II). (B) Predicted time-dependent concentrations of AB-stacked bilayer graphene (red line) and turbostratic bilayer graphene (blue line). (C) Predicted time-dependent concentrations of AB-stacked trilayer graphene (red line) and turbostratic trilayer graphene (type I, blue line; and type II, green line).

AB-stacked species and various turbostratic species generated after the dispersion is prepared (considering all possible collisions). For example, as shown schematically in Figure 7A, there is only one subtype of turbostratic bilayer graphene which is generated from the reaggregation of two monolayer graphenes. On the other hand, there are two subtypes of turbostratic trilayer graphene which are generated from the reaggregation of one monolayer graphene and one AB-stacked bilayer graphene (denoted as type I) and from the reaggregation of one monolayer graphene and one turbostratic bilayer graphene (denoted as type II). For other thicker turbostratic m-layer graphenes, there are even more possible subtypes, but here, we will only focus on bilayer and trilayer graphene since they are the most important graphene types for practical applications.

To obtain the time-dependent AB-stacked bilayer and trilayer graphene number concentrations, we can decompose $N_2(t)$ and

$N_3(t)$ as follows

$$N_2(t) = N_{2,\text{AB}}(t) + N_{2,\text{turbo}}(t) \tag{8}$$

$$N_3(t) = N_{3,\text{AB}}(t) + N^{\text{I}}_{3,\text{turbo}}(t) + N^{\text{II}}_{3,\text{turbo}}(t) \tag{9}$$

where the additional subscripts "AB" and "turbo" denote AB-stacked and turbostratic graphene, respectively, and the superscripts "I" and "II" denote type I and type II trilayer graphene, respectively. Specifically, the reaction kinetics of the generations of bilayer and trilayer graphene subtypes can be modeled as follows

$$\frac{dN_{2,\text{AB}}(t)}{dt} = -\sum_{i=1}^{M} kN_{2,\text{AB}}(t)N_i(t) \tag{10}$$

$$\frac{dN_{2,turbo}(t)}{dt} = kN_1(t)N_1(t) - \sum_{i=1}^{M} kN_{2,turbo}(t)N_i(t) \qquad (11)$$

$$\frac{dN_{3,AB}(t)}{dt} = - \sum_{i=1}^{M} kN_{3,AB}(t)N_i(t) \qquad (12)$$

$$\frac{dN_{3,turbo}^I(t)}{dt} = kN_1(t)N_{2,AB}(t) - \sum_{i=1}^{M} kN_{3,turbo}^I(t)N_i(t) \qquad (13)$$

$$\frac{dN_{3,turbo}^{II}(t)}{dt} = kN_1(t)N_{2,turbo}(t) - \sum_{i=1}^{M} kN_{3,turbo}^{II}(t)N_i(t) \qquad (14)$$

By combining eqs 8−14 with the predicted reaction rate, $k = 7.54 \times 10^{-22}$ m^3/s, obtained in Section 3.5, one can calculate the time-dependent number concentrations of various subtypes of bilayer and trilayer graphene, as shown in Figures 7B and 7C, respectively. In the case of bilayer graphene (see Figure 7B), $N_{2,turbo}(t)$ increases with time due to the reaggregation of two monolayer graphenes and then reaches a maximum in about 1 day due to the lack of source monolayer graphene, which has almost completely reaggregated with all the other species (consistent with the lifetime of 1 day for monolayer graphene, as discussed in Section 3.5). Nevertheless, the proportion of the turbostratic bilayer graphene is significantly smaller than that of the AB-stacked graphene within 1 day (at least by a factor of 20). While the proportion of turbostratic bilayer graphene becomes comparable to that of the AB-stacked graphene after 10 days, it is still smaller by a factor of 4. As a result $N_{2,AB}(t) \approx N_2(t)$ for freshly prepared bilayer graphene samples, and we conclude that the majority of the bilayer graphene in the solution is AB-stacked soon after preparation. In addition, we conclude that $N_{2,AB}(t) \approx$ 80% $N_2(t)$ after 10 days of preparation.

Similarly, as shown in Figure 7C, in the case of trilayer graphene, the concentrations of the two turbostratic subtypes, $N_{3,turbo}^I(t)$ and $N_{3,turbo}^{II}(t)$, increase with time due to the reaggregation of monolayer graphene and bilayer graphene (AB-stacked ones for type I and turbostratic ones for type II) and then reach maxima in about 2 days (for type I) and 3 days (for type II), respectively. However, note that the proportion of the type II trilayer graphene is much smaller than that of the type I species (at least by a factor of 5), as a result of the negligible proportion of its source (turbostratic bilayer graphene) compared to that of the type I species (AB-stacked bilayer graphene). In addition, contrary to the bilayer case in which the AB-stacked species always dominates the total composition, $N_{3,turbo}^I(t)$ exceeds $N_{3,AB}(t)$ by a small amount (less than a factor of 2) in about 10 days, enriching the total trilayer graphene dispersion in both AB-stacked and turbostratic species. This could probably be attributed to the high starting AB-stacked bilayer graphene composition of the dispersion after preparation.

4. CONCLUSIONS

In conclusion, we successfully combined molecular simulations, theoretical modeling, and experimental measurements to elucidate several important aspects of solution-phase exfoliated graphene aqueous dispersions. We probed experimentally and theoretically the surface coverage and electrostatic potential around a monolayer graphene−SC assembly, which exhibits a compact adsorbed monolayer of cholate ions surrounded by screening sodium counterions and ordered water molecules. The graphene surface is only partially covered by the cholate ions (∼60%), leaving many available reaction sites for potential reactants for functionalization. However, it is important to keep in mind that the graphene surface covered by charged surfactants may facilitate the adsorption of oppositely charged reactants present in the solution.[31] As a result, the impact of the graphene surface charge resulting from surfactant adsorption is also an important factor in determining the functionalization selectivity, in addition to the surface coverage. In addition, specific binding (e.g., hydrophobic bonding, hydrogen bonding, or ring stacking) between surfactants adsorbed on the graphene surface and reactants should be taken into consideration.

From the potential of mean force (PMF) calculation for two parallel graphene−SC assemblies, we found that the traditional electrostatic interaction is not the dominant contribution to the repulsive energy barrier that inhibits graphene reaggregation. Indeed, the dominant contribution is the steric hindrance induced by the last layer of cholate ions and sodium counterions confined between the two graphene sheets. Such bilayer graphene configuration corresponds to a local minimum in the PMF profile, which defines a surfactant-stabilized metastable structure for exfoliated multilayer graphene sheets. Such a metastable structure can explain experimental observations of turbostratic, non-AB-stacked graphene.[15] When using surfactants to disperse and stabilize graphene in aqueous media, one faces the following dilemma: on the one hand, surfactants can certainly stabilize graphene dispersions, but on the other hand, they prevent the formation of new AB-stacked bilayer and trilayer graphene resulting from the reaggregation process. Therefore, a possible route to obtain AB-stacked bilayer- or trilayer-enriched graphene is to pretreat the raw graphite material to establish the corresponding layering of the graphite sheets. Indeed, our recent attempt to produce bilayer- and trilayer-enriched graphene dispersions using Stage-2 GICs addresses this issue nicely.[30]

By combining the PMF results with a kinetic model of colloid aggregation, we predicted the time-dependent concentration and distribution of graphene with various layer numbers, and we further decomposed each layer type into subtypes including the AB-stacked species and various turbostratic species. This theoretical model can be very useful in estimating the lifetime of graphene dispersions. In particular, the concentrations of AB-stacked bilayer and trilayer graphene define the quality of the graphene dispersion for electronic and optical applications. Furthermore, the lifetime of monolayer graphene also influences the success of using functionalization to open their band gaps. In general, monolayer, bilayer, and trilayer graphene are easily degradable as time evolves compared to thicker multilayer graphene, and therefore, the subsequent substrate-transferring or functionalization processes should be carried out using very fresh samples to increase the yields of electronic and optical graphene devices. Our findings provide fundamental insights into the manufacturing of useful graphene-based electronic and optical devices using either functionalized monolayer graphene by controlling their surface morphology before reaction or AB-stacked multilayer graphene by controlling their layer thickness before exfoliation. Future computational work may be carried out for other effective dispersants, including surfactants (e.g., SDS, SDBS, Triton X100, and CTAB)[59] and polymers (e.g., biocompatible block copolymers).[67]

■ ASSOCIATED CONTENT

ⓢ Supporting Information. Figures of: (i) solvent accessible surface areas (SASAs) of monolayer graphene and cholate ions as a function of time (Figure S1) and (ii) cumulative average forces applied on the two parallel graphene sheets (Figure S2). Tables of: (i) summary of the simulated systems (Table S1) and (ii) summary of fitted parameters in eq S1 (Table S2). Summary of experimental procedures (Section S1), discussion of the kinetic theory of graphene aggregation (Section S2), and the complete ref 8. This material is available free of charge via the Internet at http://pubs.acs.org.

■ AUTHOR INFORMATION

Corresponding Author
dblank@mit.edu

Author Contributions
§These authors contributed equally to this work.

■ ACKNOWLEDGMENT

■ REFERENCES

(1) Novoselov, K. S.; Geim, A. K.; Morozov, S. V.; Jiang, D.; Zhang, Y.; Dubonos, S. V.; Grigorieva, I. V.; Firsov, A. A. *Science* **2004**, *306*, 666–669.

(2) Geim, A. K.; Novoselov, K. S. *Nat. Mater.* **2007**, *6*, 183–191.

(3) Novoselov, K. S.; Jiang, D.; Schedin, F.; Booth, T. J.; Khotkevich, V. V.; Morozov, S. V.; Geim, A. K. *Proc. Natl. Acad. Sci. U.S.A.* **2005**, *102*, 10451–10453.

(4) Berger, C.; Song, Z. M.; Li, X. B.; Wu, X. S.; Brown, N.; Naud, C.; Mayou, D.; Li, T. B.; Hass, J.; Marchenkov, A. N.; Conrad, E. H.; First, P. N.; de Heer, W. A. *Science* **2006**, *312*, 1191–1196.

(5) Kim, K. S.; Zhao, Y.; Jang, H.; Lee, S. Y.; Kim, J. M.; Kim, K. S.; Ahn, J. H.; Kim, P.; Choi, J. Y.; Hong, B. H. *Nature* **2009**, *457*, 706–710.

(6) Coleman, J. N. *Adv. Funct. Mater.* **2009**, *19*, 3680–3695.

(7) Park, S.; Ruoff, R. S. *Nature Nanotechnol.* **2009**, *4*, 217–224.

(8) Hernandez, Y.; et al. *Nature Nanotechnol.* **2008**, *3*, 563–568.

(9) Blake, P.; Brimicombe, P. D.; Nair, R. R.; Booth, T. J.; Jiang, D.; Schedin, F.; Ponomarenko, L. A.; Morozov, S. V.; Gleeson, H. F.; Hill, E. W.; Geim, A. K.; Novoselov, K. S. *Nano Lett.* **2008**, *8*, 1704–1708.

(10) Mohanty, N.; Berry, V. *Nano Lett.* **2008**, *8*, 4469–4476.

(11) Ohno, Y.; Maehashi, K.; Yamashiro, Y.; Matsumoto, K. *Nano Lett.* **2009**, *9*, 3318–3322.

(12) Cheng, Z. G.; Li, Q.; Li, Z. J.; Zhou, Q. Y.; Fang, Y. *Nano Lett.* **2010**, *10*, 1864–1868.

(13) Lotya, M.; Hernandez, Y.; King, P. J.; Smith, R. J.; Nicolosi, V.; Karlsson, L. S.; Blighe, F. M.; De, S.; Wang, Z. M.; McGovern, I. T.; Duesberg, G. S.; Coleman, J. N. *J. Am. Chem. Soc.* **2009**, *131*, 3611–3620.

(14) Lotya, M.; King, P. J.; Khan, U.; De, S.; Coleman, J. N. *ACS Nano* **2010**, *4*, 3155–3162.

(15) Green, A. A.; Hersam, M. C. *Nano Lett.* **2009**, *9*, 4031–4036.

(16) Green, A. A.; Hersam, M. C. *J. Phys. Chem. Lett.* **2010**, *1*, 544–549.

(17) Zhang, Y.; Tang, T.-T.; Girit, C.; Hao, Z.; Martin, M. C.; Zettl, A.; Crommie, M. F.; Shen, Y. R.; Wang, F. *Nature* **2009**, *459*, 820–823.

(18) Craciun, M. F.; Russo, S.; Yamamoto, M.; Oostinga, J. B.; Morpurgo, A. F.; Thrucha, S. *Nature Nanotechnol.* **2009**, *4*, 383–388.

(19) Faugeras, C.; Nerriere, A.; Potemski, M.; Mahmood, A.; Dujardin, E.; Berger, C.; de Heer, W. A. *Appl. Phys. Lett.* **2008**, *92*, 011914.

(20) Castro Neto, A. H.; Guinea, F.; Peres, N. M. R.; Novoselov, K. S.; Geim, A. K. *Rev. Mod. Phys.* **2009**, *81*, 109.

(21) dos Santos, J. M. B. L.; Peres, N. M. R.; Castro, A. H. *Phys. Rev. Lett.* **2007**, *99*, 256802.

(22) Dresselhaus, M. S.; Dresselhaus, G. *Adv. Phys.* **1981**, *30*, 139–326.

(23) Li, X. L.; Zhang, G. Y.; Bai, X. D.; Sun, X. M.; Wang, X. R.; Wang, E.; Dai, H. J. *Nature Nanotechnol.* **2008**, *3*, 538–542.

(24) Ang, P. K.; Wang, S.; Bao, Q. L.; Thong, J. T. L.; Loh, K. P. *ACS Nano* **2009**, *3*, 3587–3594.

(25) Lee, J. H.; Shin, D. W.; Makotchenko, V. G.; Nazarov, A. S.; Fedorov, V. E.; Kim, Y. H.; Choi, J. Y.; Kim, J. M.; Yoo, J. B. *Adv. Mater.* **2009**, *21*, 1–5.

(26) Li, X. L.; Wang, X. R.; Zhang, L.; Lee, S. W.; Dai, H. J. *Science* **2008**, *319*, 1229–1232.

(27) Behabtu, N.; Lomeda, J. R.; Green, M. J.; Higginbotham, A. L.; Sinitskii, A.; Kosynkin, D. V.; Tsentalovich, D.; Parra-Vasquez, A. N. G.; Schmidt, J.; Kesselman, E.; Cohen, Y.; Talmon, Y.; Tour, J. M.; Pasquali, M. *Nature Nanotechnol.* **2010**, *5*, 406–411.

(28) Zheng, J. A.; Di, C. A.; Liu, Y. Q.; Liu, H. T.; Guo, Y. L.; Du, C. Y.; Wu, T.; Yu, G.; Zhu, D. B. *Chem. Commun.* **2010**, *46*, 5728–5730.

(29) Lee, J. H.; Shin, D. W.; Makotchenko, V. G.; Nazarov, A. S.; Fedorov, V. E.; Yoo, J. H.; Yu, S. M.; Choi, J. Y.; Kim, J. M.; Yoo, J. B. *Small* **2010**, *6*, 58–62.

(30) Shih, C.-J.; Vijayaraghavan, A.; Krishnan, R.; Sharma, R.; Han, J.-H.; Ham, M.-H.; Jin, Z.; Lin, S.; Paulus, G. L. C.; Reuel, N. F.; Wang, Q. H.; Blankschtein, D.; Strano, M. S. *Nature Nanotechnol.* **2011**, *6*, 439–445.

(31) Sharma, R.; Baik, J. H.; Perera, C. J.; Strano, M. S. *Nano Lett.* **2010**, *10*, 398–405.

(32) Lomeda, J. R.; Doyle, C. D.; Kosynkin, D. V.; Hwang, W. F.; Tour, J. M. *J. Am. Chem. Soc.* **2008**, *130*, 16201–16206.

(33) Nair, N.; Kim, W. J.; Usrey, M. L.; Strano, M. S. *J. Am. Chem. Soc.* **2007**, *129*, 3946–3954.

(34) Usrey, M. L.; Lippmann, E. S.; Strano, M. S. *J. Am. Chem. Soc.* **2005**, *127*, 16129–16135.

(35) Sammalkorpi, M.; Panagiotopoulos, A. Z.; Haataja, M. *J. Phys. Chem. B* **2008**, *112*, 2915–2921.

(36) Tummala, N. R.; Striolo, A. *J. Phys. Chem. B* **2008**, *112*, 1987–2000.

(37) Tummala, N. R.; Striolo, A. *Phys. Rev. E* **2009**, *80*, 021408.

(38) Shih, C.-J.; Lin, S.; Strano, M. S.; Blankschtein, D. *J. Am. Chem. Soc.* **2010**, *132*, 14638–14648.

(39) Hess, B.; Kutzner, C.; van der Spoel, D.; Lindahl, E. *J. Chem. Theory Comput.* **2008**, *4*, 435–447.

(40) Cheng, A.; Steele, W. A. *J. Chem. Phys.* **1990**, *92*, 3858–3866.

(41) Berendsen, H. J. C.; Grigera, J. R.; Straatsma, T. P. *J. Phys. Chem.* **1987**, *91*, 6269–6271.

(42) Jorgensen, W. L.; Maxwell, D. S.; Tirado-Rives, J. *J. Am. Chem. Soc.* **1996**, *118*, 11225–11236.

(43) Lin, S.; Blankschtein, D. *J. Phys. Chem. B* **2010**, *114*, 15616–15625.

(44) Miyamoto, S.; Kollman, P. A. *J. Comput. Chem.* **1992**, *13*, 952–962.

(45) Hess, B. *J. Chem. Theory Comput.* **2008**, *4*, 116–122.

(46) Darden, T.; York, D.; Pedersen, L. *J. Chem. Phys.* **1993**, *98*, 10089–10092.

(47) Essmann, U.; Perera, L.; Berkowitz, M. L.; Darden, T.; Lee, H.; Pedersen, L. G. *J. Chem. Phys.* **1995**, *103*, 8577–8593.

(48) Bussi, G.; Donadio, D.; Parrinello, M. *J. Chem. Phys.* **2007**, *126*, 014101.

(49) Berendsen, H. J. C.; Postma, J. P. M.; Vangunsteren, W. F.; Dinola, A.; Haak, J. R. *J. Chem. Phys.* **1984**, *81*, 3684–3690.

(50) Sasaki, Y.; Nagata, H. D.; Fujii, Y. K.; Lee, S.; Nagadome, S.; Sugihara, G. *Colloids Surf. B* **1997**, *9*, 169–176.

(51) Israelachvili, J. N. *Intermolecular and surface forces*; Academic Press: London, 1991.

(52) Gurtovenko, A. A.; Vattulainen, I. *J. Chem. Phys.* **2009**, *130*, 215107.

(53) Xu, Z. J.; Yang, X. N.; Yang, Z. *Nano Lett.* **2010**, *10*, 985–991.

(54) Ingle, J. D.; Crouch, S. R. *Spectrochemical analysis*; Prentice Hall: Englewood Cliffs, N.J., 1988.

(55) Tanford, C. *The hydrophobic effect: formation of micelles and biological membranes*, 2nd ed.; Krieger: Malabar, 1991.

(56) Choudhury, N.; Pettitt, B. M. *J. Am. Chem. Soc.* **2005**, *127*, 3556–3567.

(57) Knecht, V.; Risselada, H. J.; Mark, A. E.; Marrink, S. J. *J. Colloid Interface Sci.* **2008**, *318*, 477–486.

(58) Hiemenz, P. C.; Rajagopalan, R. *Principles of colloid and surface chemistry*, 3rd ed.; Marcel Dekker: New York, 1997.

(59) Smith, R. J.; Lotya, M.; Coleman, J. N. *New J. Phys.* **2010**, *12*, 125008.

(60) Khair, A. S.; Squires, T. M. *J. Fluid Mech.* **2009**, *640*, 343–356.

(61) Hui, Z. *J. Phys. Chem. C* **2010**, *114*, 8389–8397.

(62) Israelachvili, J. N. *Philos. Mag. A* **1981**, *43*, 753–770.

(63) Horn, R. G.; Israelachvili, J. N. *J. Chem. Phys.* **1981**, *75*, 1400–1411.

(64) Israelachvili, J. N.; Tandon, R. K.; White, L. R. *J. Colloid Interface Sci.* **1980**, *78*, 430–443.

(65) Pashley, R. M.; Israelachvili, J. N. *Colloids Surf.* **1981**, *2*, 169–187.

(66) Fuchs, N. *Z. Phys. Chem., Abt. A* **1934**, *171*, 199–208.

(67) Seo, J. W. T.; Green, A. A.; Antaris, A. L.; Hersam, M. C. *J. Phys. Chem. Lett.* **2011**, *2*, 1004–1008.